Spin-dependent Electron Scattering from Polarized Protons and Deuterons with the BLAST Experiment at MIT-Bates

Douglas K. Hasell, Richard G. Milner, and Robert P. Redwine

Massachusetts Institute of Technology, Cambridge, MA, 02139

Ricardo Alarcon

Arizona State University, Tempe, AZ, 85287

Haiyan Gao

Duke University, Durham, NC, 27708

Michael Kohl

Hampton University, Hampton, VA, 23668

John R. Calarco

University of New Hampshire, Durham, NH, 03824

Annu. Rev. Nucl. Part. Sci. 2010 61 1056-8700/97/0610-00

Key Words BLAST Experiment, Proton Form Factor, Neutron Form Factor, Deuteron Form Factor, Few-body Structure

Abstract

The Bates Large Acceptance Spectrometer Toroid (BLAST) experiment was operated at the MIT-Bates Linear Accelerator Center from 2003 until 2005. The experiment was designed to exploit the power of a polarized electron beam incident on polarized targets of hydrogen and deuterium to measure, in a systematic manner, the neutron, proton, and deuteron form factors as well as other aspects of the electromagnetic interaction on few-nucleon systems. A brief description of the experiment is provided, together with presentation and discussion of the numerous results obtained.

CONTENTS

Introduction 3

The BLAST Experiment 6

Nucleon Form Factors 10

Proton Form Factors 13

Neutron Electric Form Factor G_E^n 17

Fourier Transforms of Nucleon Form Factors 21

The Structure of the Deuteron from Elastic Electron Scattering 22

Electro-disintegration of the Deuteron with Detection of an Emitted Proton 28

Summary and Conclusions 31

Acknowledgments 31

1 Introduction

Understanding the fundamental structure of matter in the universe, both visible and dark, is a central thrust of physics. The mass of the visible matter is almost entirely contained in the form of atomic nuclei. The structure and properties of atomic nuclei are successfully explained by strong interactions among the constituent protons and neutrons using quantum many-body theory. The Standard Model theory of the strong interaction, Quantum Chromodynamics (QCD), provides a successful, fundamental description of the protons and neutrons in terms of the interactions between light, point-like quarks via colored, massless gluons. Unfortunately, at this time exact solutions of QCD in the non-perturbative regime, *i.e.* at the relatively low energy scales of the universe around us, are not available. Thus, progress in seeking a fundamental explanation of elementary properties of the proton and neutron, *e.g.* mass, spin, distribution of charge and magnetism, in terms of quarks and gluons relies on QCD-inspired models, lattice gauge theory, and of course experiment.

Experimentally, the structure of the nucleon is best elucidated in terms of its constituents by means of lepton scattering, which utilizes the electroweak force, the most precisely tested interaction in physics. Elastic electron-nucleon scattering, where the final-state electron and nucleon are the same as in the initial state, is the most basic process to study hadron structure. Described by a perturbative expansion in powers of $\alpha_{_{EM}}$, in leading order the cross section is well described by single-photon exchange and the definition of two functions, known as elastic form factors, which describe the distribution of charge and magnetism. The Sachs form factors, denoted as the electric $G_E(Q^2)$ and magnetic $G_M(Q^2)$, are defined for both the proton and the neutron and are functions of the four-momentum transfer squared, Q^2.

Since the 1960's the proton elastic form factors have been well determined at low and moderate Q^2. However, the determination of the neutron form factors was problematic. Nature does not provide a free neutron target, so experiments were carried out to measure the cross section in quasi-elastic $(e, e'n)$ scattering from the deuteron. However, the determination of the neutron elastic form factors was plagued by systematic uncertainties. Experimentally, electron beams were pulsed with a duty factor typically no higher than 1 %, so poor signal-to-background was a strong limitation. Further, the neutron in the deuteron is not at rest but has Fermi motion, which produces both momentum-dependent and binding effects. In addition, at high neutron momenta, the effect of the D-state of the deuteron is sizable. In particular, the determination of the intrinsically small neutron electric form factor $G_E^n(Q^2)$ was highly uncertain. For over fifty years, a major goal of electromagnetic nuclear physics was the determination of the neutron charge distribution with precision comparable to that of the proton.

Sophisticated theoretical frameworks have been developed to describe electron scattering from few-body nuclei at low Q^2. For example, at $Q^2 \leq 0.5$ (GeV/c)^2, the theory of Arenhövel and colleagues [1–5] successfully describes cross section data. Effective field theory [6, 7] has also been applied to tensor polarization observables at low momentum. Precise and complete measurements of polarization observables in elastic and quasi-elastic scattering from deuterons can provide new and stringent tests of more subtle aspects of theoretical models, *e.g.* D-state, choice of nucleon-nucleon potential, relativistic corrections, *etc.*

The MIT-Bates South Hall Ring (SHR [8]) and the experiment described here were designed and constructed with the express goal of overcoming previous limitations in the determination of the proton and neutron form factors by carrying out a systematic and complete set of measurements on few-body systems. The essential technique was the use of polarization observables to reduce systematic uncertainties in determining small components of the interaction cross section. The SHR provided a 100 % duty-factor highly polarized, intense electron beam at an energy of 850 MeV. The Bates Large Acceptance Spectrometer Toroid (BLAST [9]) was designed for optimally study of few-body systems like the deuteron using polarized beams and targets by detecting the important channels simultaneously over a large kinematic range. This allowed for an understanding of the nucleon structure dependence which was essential to minimizing uncertainties in the precise determination of the neutron electric form factor. In parallel, important new measurements to constrain the structure of the deuteron were carried out.

BLAST used an internal, highly polarized, gas target of hydrogen and deuterium which offered great advantage in the control of systematic uncertainties. This configuration approached the ideal of pure scattering of the lepton from the polarized nucleus without dilution. Also, the spin direction could be easily changed to optimize sensitivity to the interesting physics and it was possible to cycle rapidly between vector and tensor polarization of the deuteron.

The BLAST experiment was constructed in the years 1998 through 2002, was commissioned in 2003 and the data presented here were acquired in the period November 2003 through June 2005. Integrated luminosities of 500 pb^{-1} and 94 pb^{-1} were recorded on vector and tensor polarized deuterium and polarized hydrogen, respectively.

In total eleven PhD theses were produced from analysis of the BLAST experimental data. Results from some of those theses are included in the following sections: Section 3.1 [10, 11], Section 3.2 [12, 13], Section 4 [14, 15], and Section 5 [16, 17]. The remaining theses [18–20] addressed topics beyond the scope of this review.

2 The BLAST Experiment

The BLAST experiment [21] was designed to exploit the power of a highly polarized electron beam incident on highly polarized targets of hydrogen and deuterium to measure the form factors of the proton, neutron, and deuteron in a precise and systematic manner.

The experiment was situated on the South Hall Ring, SHR, of the MIT-Bates Linear Accelerator Center (Figure 1). The accelerator consisted of a polarized electron source followed by a 500 MeV linac with a recirculator which injected longitudinally polarized electrons into the SHR.

Polarized electrons were produced by laser photoemission on a strained, highly doped, $\mathrm{GaAs_{0.95}P_{0.05}}$ photocathode [22]. Typical polarizations were ~ 70 %. Beam helicity was changed for each fill by reversing the laser polarization.

For BLAST a beam energy of 850 MeV was chosen. The stored current was typically > 200 mA with a lifetime > 25 minutes. The beam current was measured using a parametric direct current transformer in the ring. Beam polarization in the ring was ~ 66 %. A Siberian Snake on the SHR opposite BLAST maintained the longitudinal polarization at the BLAST target. A Compton polarimeter [23] upstream of the detector measured the beam polarization, P_e, for each run with a precision of ~ 4 %. The polarizations for the different beam helicities were the same to < 1 %.

An atomic beam source (ABS [24]) produced highly polarized proton (vector) or deuteron (vector and tensor) targets. The ABS (Figure 2) consisted of an RF dissociator to produce atomic hydrogen or deuterium, followed by two sets of permanent sextupole magnets which focused the atomic beam into the target cell. Three RF transition units in combination with variable magnets were used to populate the desired spin states. The target cell was a 60 cm long, 1.5 cm diameter, open-ended, tube made of 50 μm aluminum, aligned with the beam and centered at the interaction point. This provided an isotopically pure, polarized target without entrance or exit windows, minimizing background. The target cell was coated with Drifilm to reduce depolarization and cooled to $\sim$ 100K to increase the target density.

A holding field around the target cell defined the nominal spin direction as $31.3^\circ \pm 0.43^\circ$ in 2004 and $47.4^\circ \pm 0.45^\circ$ in 2005 in the horizontal plane of the left sector. Thus, electrons scattered into the left sector had momentum transfers roughly perpendicular to the spin direction, while electrons scattered into the right sector had momentum transfers roughly parallel to the spin direction.

Target polarizations were determined from different experimental asymmetry measurements and the beam polarization, P_e, was measured by the Compton polarimeter. The polarizations achieved were typically $P_z \approx 83$ % for the proton (see Section 3.1) and $P_z \approx 89$ % (79 %) (see Section 5) and $P_{zz} \approx 69$ % (55 %) (see Section 4) in 2004 (2005) for the deuteron. The target areal density was typically $\sim 7 \times 10^{13}$ atoms/cm^2 for both hydrogen and deuterium.

The BLAST experiment utilized a left/right symmetric, large acceptance, general purpose detector (Figure 3) to identify and measure the scattered particles. The detector was based upon an eight sector, toroidal, magnetic field. The two horizontal sectors were instrumented with detector components, while the two vertical sectors were used for the internal gas target and to pump the beamline. The detector was left/right symmetric with the exception of the neutron detectors, which were enhanced in the right sector to aid the measurement of G_E^n. Each sector included drift chambers for tracking, aerogel Čerenkov detectors to discriminate between electrons and pions, time-of-flight scintillators to determine the relative timing of the reaction products and provide the trigger timing, and thick walls of plastic scintillators to identify neutrons using time-of-flight.

The eight-sector toroidal magnet was chosen to minimize the effect on the beam transport, to have a small gradient at the polarized target, and to stop low energy particles from reaching the detectors. The field was however not uniform in the tracking region with a maximum field of ~ 3.8 kG. The field was measured on a 5 cm, three-dimensional grid which was used in track reconstruction.

The wire chambers measured the momenta, charges, scattering angles, and production vertices of the emitted charged particles. The wire chambers nominally subtended the polar angular range $20°$–$80°$ and $\pm 15°$ in azimuth. Each sector contained three drift chambers joined to form a single gas volume to minimize multiple scattering. The drift chambers achieved a momentum resolution of ~ 3 % with a vertex resolution of ~ 1 cm, and an angular resolution of $\sim 0.5°$ in both polar and azimuthal angles. The drift chambers also served as a highly effective proton veto in identifying neutrons.

Behind the drift chambers were aerogel Čerenkov detectors [25]. used to discriminate between pions and electrons. A 89 % efficiency was achieved.

The time-of-flight, TOF, detector consisted of vertical scintillator bars with photomultiplier tubes (PMTs) at both ends. These provided a fast, stable timing signal correlated with the time of each event at the target, independent of which scintillator bar was struck. This was used to trigger the readout and data acquisition system for all other components. An intrinsic time resolution of 320 ± 44 ps was measured for the 32 TOF detectors with an efficiency better than 99 %.

Thick scintillator bars with PMTs at both ends were used to detect neutrons. The arrangement was asymmetric with larger and thicker (more efficient) coverage in the right sector to improve the measurement of G_E^n.

A laser flasher system was connected to all PMT based detectors to monitor the timing stability during the experiment.

A multi-level, general purpose trigger and buffered data acquisition system allowed data to be accumulated simultaneously for different physics reactions. Event rates up to 1.4 kHz (0.2–0.8 kHz typical), with an event size of ~ 1.5 kB, were possible with deadtime less than 10 %.

During normal operation the accelerator, target, detector, and data acquisition operated almost automatically, requiring very little human intervention. When the current in the SHR dropped below a preset limit, the data acquisition system would stop taking data and ramp down the high voltage. Then the beam in the SHR would be dumped and a new injection started. Once sufficient current was stored, high voltage would be ramped up and data taking would resume. Typically, the downtime was about 90 seconds with data-taking period of 10 minutes. The beam helicity was reversed for each fill. Every 5 minutes the target spin states were randomly cycled. The ABS would inhibit data acquisition for the ~ 2 seconds required for the transition.

Periodically runs were taken with an empty target or using an unpolarized gas system to determine contributions from background and false asymmetries. Cosmic ray data were also collected and used to check relative timing between detectors.

3 Nucleon Form Factors

Spin degrees of freedom have opened new opportunities in the study of the structure of the nucleon, a subject of fundamental importance to the ultimate understanding of how quantum chromodynamics (QCD) works in the non-perturbative region. Among quantities describing the structure of the nucleon, the electromagnetic form factors are the most basic and fundamental quantities - they are sensitive to the distribution of charge and magnetization within the nucleon. At low four-momentum transfer squared Q^2, they are sensitive to the pion cloud [26–31], and provide tests of effective field theories of QCD based on chiral symmetry [32, 33]. Lattice QCD calculations continue to make advances in techniques [34–36] and computing power, and tests against precise nucleon form factor data will be possible in the future. Accurate measurements of nucleon electromagnetic form factors at low Q^2 are also important for the interpretation of parity-violating electron scattering experiments [37, 38], which probe the strange quark contribution to the nucleon electromagnetic structure. In the limit of $Q^2 \to 0$, the charge and magnetic radii of the nucleon can be determined from the slope of the corresponding electric or magnetic form factor. Precise information about the proton charge radius is particularly important because it is a crucial input to high-precision tests of QED based on hydrogen Lamb shift measurements. The subject of the charge radius of the proton has received a lot of attention recently because a new experiment [39] reported a much smaller value of the proton charge radius, from a measurement of the Lamb shift in muonic hydrogen atoms, than the CODATA value [40] extracted from Lamb shift measurements of hydrogen atoms. The new experiment of muonic hydrogen Lamb shift has an unprecedented precision of 0.1 %. The experimental situation becomes more interesting as the latest value of the charge radius of the proton determined from an electron scattering experiment [41] is in agreement with the CODATA value [40].

The proton electric (G_E^p) and magnetic (G_M^p) form factors have been studied extensively in the past [42–44] over a wide range of Q^2 from unpolarized electron-proton elastic scattering using the Rosenbluth separation technique [45]. It is also interesting to study the ratio $\mu_p G_E^p / G_M^p$ as a function of Q^2, where $\mu_p \sim 2.79$ is the proton magnetic moment in units of nuclear magnetons. The observation of a Q^2 dependence in the form factor ratio would suggest different charge and current spatial distributions inside the proton. The unpolarized data are consistent with $\mu_p G_E^p / G_M^p \sim 1$ up to $Q^2 \approx 6$ (GeV/c)^2 [46, 47].

Recent advances in polarized beams, targets, and polarimetry have made possible a new class of experiments extracting $\mu_p G_E^p / G_M^p$ utilizing double polarization observables. The spin-dependent cross section has an interference term between G_E^p and G_M^p, allowing for a direct determination of $\mu_p G_E^p / G_M^p$ from either the spin-dependent asymmetry [48] or the recoil polarization measurement [49] at a single beam energy and scattering angle. The measurement of polarization observables avoids uncertainties due to detector acceptance, efficiency and luminosity, which are major sources of systematic errors in unpolarized experiments.

Data from polarization transfer experiments [50, 51] show an intriguing behavior at higher Q^2: starting at $Q^2 \approx 1$ (GeV/c)^2, $\mu_p G_E^p / G_M^p$ drops linearly from approximately unity down to 0.28 at the highest measured Q^2 value ($\sim$ 5.64 (GeV/c)^2). This trend continues as shown by the latest measurement [52] of this ratio, using the same experimental technique to a Q^2 value of 8.5 (GeV/c)^2. This is inconsistent with previous results [46, 47] using unpolarized beams, verified by recent unpolarized-beam experiments [53, 54]. While the high Q^2 data on $\mu_p G_E^p / G_M^p$ from recoil polarization experiments [50, 51] have been described in terms of nonzero parton orbital angular momentum or hadron helicity flip [29, 30, 55–59], it is important to understand the discrepancy between results obtained from recoil proton polarization measurements and those from the Rosenbluth method. Calculations of the two-photon exchange (TPE) contribution are able to explain part of the observed discrepancy [60–63]. The predicted TPE contribution has a large effect on Rosenbluth extractions, but only a minor effect on polarized experiments. The BLAST Collaboration carried out a first measurement [64] of this form factor ratio employing a pure polarized hydrogen internal gas target, the results of which are presented in Section 3.1. Future high-precision measurements of the proton form factor ratio, in combination with precise differential cross section data in the $Q^2 \to 0$ region, will allow for separate determinations of the proton form factors and, therefore, a better determination of the proton charge radius.

In the absence of a free neutron target, measurements of neutron electromagnetic form factors are more difficult than their proton counterparts. Determinations of the neutron electric (G_E^n), and magnetic (G_M^n) form factors at finite Q^2 are typically carried out using quasi-elastic electron scattering from deuterium or ^{3}He targets. While inclusive polarized $^3\vec{H}e(\vec{e}, e')$ [65–67] and $^2\vec{H}(\vec{e}, e')$ at quasi-elastic kinematics have provided precision data on G_M^n at low values of Q^2, the unpolarized coincidence ratio technique of $\frac{^2H(e,e'n)}{^2H(e,e'p)}$ has been extended recently up to a Q^2 value of 4.8 (GeV/c)^2 [68] in the determination of G_M^n. While the slope of $G_E^n(Q^2)$ at $Q^2 = 0$, which defines the square of the neutron charge radius, has been determined precisely by the scattering of thermal neutrons from atomic electrons [69], compared to G_M^n, the determination of neutron electric form factor is more challenging due to the much smaller value of G_E^n. Despite this fact, it can be obtained with high precision from double-polarization observables based on the interference of G_E^n with G_M^n. With the availability of high-duty-factor polarized electron beams over the last decade, experiments [70–76] have employed recoil polarimeters, and targets of polarized ^{2}H and ^{3}He to carry out precision measurements of G_E^n using polarization techniques with inherently small systematic uncertainties. Recently, the measurement of G_E^n using the reaction of $^3\vec{H}e(\vec{e}, e'n)$ in quasi-elastic kinematics has been extended to a Q^2 value of 3.4 (GeV/c)^2. In Section 3.2 the BLAST results on G_E^n from quasi-elastic $^2\vec{H}(\vec{e}, e'n)$ reactions will be presented.

3.1 Proton Form Factors

In the one-photon-exchange approximation, the elastic scattering asymmetry of longitudinally polarized electrons from polarized protons with respect to the electron beam helicity has the form [48]

$$A_{phys} = \frac{v_z \cos\theta^* {G_M^p}^2 + v_x \sin\theta^* \cos\phi^* G_M^p G_E^p}{(\tau {G_M^p}^2 + \epsilon {G_E^p}^2) \,/\, [\epsilon(1+\tau)]} \tag{1}$$

where θ^* and ϕ^* are the polar and azimuthal angles of the target polarization defined relative to the three-momentum transfer vector of the virtual photon, and $\tau = Q^2/(4M_p^2)$ with the proton mass M_p. The longitudinal polarization of the virtual photon is denoted as $\epsilon = [1 + 2(1+\tau)\tan^2(\theta_e/2)]^{-1}$, where θ_e is the electron scattering angle, and $v_z = -2\tau\tan(\theta_e/2)\sqrt{1/(1+\tau)+\tan^2(\theta_e/2)}$ and $v_x = -2\tan(\theta_e/2)\sqrt{\tau/(1+\tau)}$ are kinematic factors. The experimental asymmetry

$$A_{exp} = P_e P_z \, A_{phys} \tag{2}$$

is reduced by the beam (P_e) and target (P_z) polarizations.

The form factor ratio $\mu_p G_E^p/G_M^p$ and the polarization product $P_e P_z$ can be determined separately from two experimental asymmetries, A_l and A_r, measured simultaneously at the same Q^2 value, but with different spin orientations (θ_l^*, ϕ_l^*) and (θ_r^*, ϕ_r^*), respectively, by using a detector with left and right sectors symmetric about the incident electron beam. For a target polarization angle oriented $\sim 45°$ to the left of the beam, A_l (A_r) is predominantly transverse (longitudinal) to the direction of momentum transfer.

During the BLAST experiment, $\vec{\mathrm{H}}(\vec{e}, e'p)$ data were acquired for a total integrated charge of 298 kC on the target. The elastic events were selected with a cut on the invariant mass of the virtual photon and the target proton system, fiducial cuts on the polar and azimuthal acceptance, and cuts on the position of the electron and proton vertex in the target cell. Separate yields σ_{ij} were analyzed for each combination of electron helicity i and target spin state j, normalized to the integrated beam current. The event-weighted $\langle Q^2 \rangle$ was formed from the average of $\langle Q_e^2 \rangle$ (determined from the electron scattering angle) and $\langle Q_p^2 \rangle$ (from the proton recoil angle) in each bin. The yield distributions were in good agreement with results from a Monte Carlo simulation that included all detector efficiencies.

The experimental double asymmetry was formed from

$$\frac{\sigma_{++} - \sigma_{+-} - \sigma_{-+} + \sigma_{--}}{\sigma_{++} + \sigma_{+-} + \sigma_{-+} + \sigma_{--}} \tag{3}$$

The beam and target single-spin asymmetries were also analyzed and served as a monitor of false asymmetries, which were found to be negligible. The experimental asymmetry was corrected for dilution by unpolarized background. Radiative corrections were also applied using the code MASCARAD [77], but were less than 0.43 % for A_r and 0.16 % for A_l.

To extract the form factor ratio, the experimental asymmetries A_l and A_r were interpolated in each Q^2 bin to the average value of $\langle Q^2 \rangle$ in the left and right sectors (a correction of less than 0.25 %). As discussed previously, the polarization product $P_e P_z$ and the form factor ratio $\mu_p G_E^p / G_M^p$ could be determined from the measured asymmetries A_l and A_r using Eqs. (1), (2). In this way the so-called super ratio A_l/A_r yielded $\mu_p G_E^p / G_M^p$ and $P_e P_z$ independently for each Q^2 bin. The eight values of $P_e P_z$ extracted in this manner were self-consistent. The final analysis was done with a 9-parameter fit (8 values of $\mu_p G_E^p / G_M^p$ and a single value of $P_e P_z$) to the 16 asymmetries for optimal extraction of the form factor ratio [10] (consistent with the super-ratio analysis), resulting in $P_e P_z = 0.537 \pm 0.003$ (stat) $\pm$ 0.007 (sys).

The dominant source of systematic uncertainty was the determination of $\langle Q^2 \rangle$. This was estimated from the difference between $\langle Q_e^2 \rangle$ and $\langle Q_p^2 \rangle$ to be less than 0.002 $(\text{GeV/c})^2$. The correlation is unknown since different regions of the spectrometer were used for each Q^2 bin. The event-weighted average spin angle of the target with respect to the beam was $48.0° \pm 0.4°(\text{stat}) \pm 0.3°(\text{sys})$, extracted from the analysis of the T_{20} tensor analyzing power in elastic scattering from deuterium in combination with a careful mapping of the magnetic field in the target region [14]. The resulting systematic uncertainty in $\mu_p G_E^p / G_M^p$ was less than 0.35 % because of reduced sensitivity to the target spin angle uncertainty due to a compensation in the simultaneous extraction of $P_e P_z$. All other systematic uncertainties including Coulomb distortion were negligible, and more details can be found in Refs. [10, 64].

The results are displayed in Figure 4 with the inner error bars due to statistical uncertainties and the outer error bars being the total (statistical and systematic contributions added in quadrature). Also shown in Figure 4 are published recoil polarization data [50, 51, 78–81], together with a few selected models discussed in [42]: a soliton model [82]; a relativistic constituent quark model (CQM) with SU(6) symmetry breaking and a constituent quark form factor [83], an extended vector meson dominance model [84], an updated dispersion model [85], and a Lorentz covariant chiral quark model [26]. We also show the parameterizations by Friedrich and Walcher [27] and Kelly [31].

The impact of the BLAST results on the separated proton charge and magnetic form factors normalized to the dipole form factor $G_D = (1 + Q^2/0.71)^{-2}$ is illustrated in Figure 5. In this figure, Rosenbluth extractions of G_E^p and G_M^p from single experiments [46, 53, 86–91] are presented as open triangles with statistical and total error bars, the systematic errors added in quadrature. The combined cross section data [53, 86–88, 90–94], obtained from [90, 95], were binned to obtain a single longitudinal-transverse (L-T) separation of G_E^p and G_M^p at each of the BLAST kinematics (blue circles). In comparison, the red squares show the form factors extracted by combining the unpolarized cross section data and the measured form factor ratio from BLAST. By including the BLAST data not only are the uncertainties reduced by a factor of 1.3–2.5, but also the negative correlation between G_E^p and G_M^p typical of L-T separations is greatly reduced.

The extracted form factor ratio ($\mu_p G_E^p/G_M^p$) in our experiment is consistent with unity. The most recent unpublished data [96] from a proton recoil polarization measurement in a similar Q^2 range show a different Q^2 dependence in the form factor ratio from that of our BLAST results. Further experimental investigations are necessary to understand this difference. The separated form factors from BLAST may suggest a deviation from the dipole form below 1 $(\mathrm{GeV/c})^2$, particularly around $Q^2 \approx 0.3$ to 0.4 $(\mathrm{GeV/c})^2$, similar to what has been observed in the neutron magnetic form factor data [65–67]. Interestingly, the neutron electric form factor values [70–72] peak in a similar Q^2 region. A possible explanation for this observation could be a manifestation of the pion cloud at low momentum transfer [26, 27]. However, more precise data and a more detailed theoretical understanding of the pion cloud effect are necessary before one can confirm and quantify such an effect.

3.2 Neutron Electric Form Factor G_E^n

High precision determinations of G_E^n at finite Q^2 are typically obtained from double-polarization observables using quasi-elastic electron scattering from deuteron or ^{3}He targets.

The differential cross section for the $^2\vec{H}(\vec{e},e'n)$ reaction with polarized beam and target can be written [48, 97]

$$d^3\sigma/(d\Omega_e d\Omega_{pq} d\omega) \;=\; \sigma_0(1+\Sigma+P_e\Delta) \tag{4}$$

with

$$\begin{aligned} \Sigma &= \sqrt{\frac{3}{2}}P_z A_d^V + \sqrt{\frac{1}{2}}P_{zz}A_d^T \\ \Delta &= A_e + \sqrt{\frac{3}{2}}P_z A_{ed}^V + \sqrt{\frac{1}{2}}P_{zz}A_{ed}^T, \end{aligned} \tag{5}$$

where σ_0 is the unpolarized differential cross section, $P_z = n_+ - n_-$ and $P_{zz} = n_+ + n_- - 2n_0$ are the vector and tensor polarizations of the deuteron target defined by the relative populations n_m of the three deuteron magnetic sub-states with respect to the deuteron orientation axis, $m = +1, 0, -1$, respectively, and P_e is the longitudinal polarization of the electron beam.

With BLAST all of the polarization observables A_i in Eq. (5) have been measured in a single experiment. The beam-target vector polarization observable A_{ed}^V is particularly sensitive to the neutron form factor ratio G_E^n/G_M^n [98]. In the Plane Wave Born Approximation (PWBA), and with the deuteron in a pure S-state, the asymmetry A_{ed}^V can be written analogously to elastic scattering from the free neutron as

$$\begin{aligned} A_{ed}^V &= \frac{a\,{G_M^n}^2\cos\theta^* + b\,G_E^n G_M^n \sin\theta^*\cos\phi^*}{c\,{G_E^n}^2 + {G_M^n}^2} \\ &\approx a\cos\theta^* + b\,\frac{G_E^n}{G_M^n}\sin\theta^*\cos\phi^*, \end{aligned} \tag{6}$$

where θ^* and ϕ^* are the target spin orientation angles with respect to the momentum transfer vector and a, b, and c are known kinematic factors. This asymmetry has the largest sensitivity to G_E^n when the momentum transfer vector is perpendicular to the target polarization, *i.e.* $\theta^* = 90°$.

The experimental value of the beam-vector polarization observable A_{ed}^V can be written as:

$$A_{ed}^V = \sqrt{\frac{3}{2}}\frac{1}{P_e P_z}\frac{Y_{++} + Y_{--} - Y_{+-} - Y_{-+}}{Y_{tot}}, \tag{7}$$

where Y_{tot} is the total yield obtained by summing up all six combinations hm.

The experimental asymmetries were compared to Monte Carlo simulations based on the deuteron electro-disintegration model [97], for which events were generated according to the unpolarized cross section and weighted event-by-event with the spin-dependent terms in Eq. (5). The model includes the corrections to the asymmetry in Eq. (6) due to final state interactions (FSI), the relative contributions of meson exchange currents (MEC), isobar configurations (IC) and relativistic corrections (RC). The acceptance-averaged asymmetry A_{ed}^V was simulated for different values of G_E^n/G_M^n and compared to the experimental values. In order to extract the best value of the form factor ratio for each Q^2 bin, a χ^2 minimization was performed independently with respect to the missing momentum of the reaction and the angle of the neutron in the hadronic center-of-mass system. Both extractions produced consistent results.

Figure 6 displays the measured values of A_{ed}^V and A_d^T with Monte Carlo simulations based on the deuteron electro-disintegration model of Arenhövel [97] (dotted magenta = PWBA, short-dashed green = PWBA+FSI, solid red = PWBA+FSI+MEC+IC+RC) using standard parameterizations for the nucleon form factors. In addition, the corresponding curves for $G_E^n \equiv 0$ (dash-dotted red) and for elastic scattering from the free neutron (dashed black line) are shown. The asymmetries A_e, A_d^V, and A_{ed}^T all vanish in the Born approximation due to parity and time reversal conservation and remain very small (below 1 %) even in the presence of FSI. The calculations use the standard dipole form factor $G_D = (1 + Q^2/0.71)^{-2}$ for G_E^p, G_M^p/μ_p, and G_M^n/μ_n, and $1.91\tau/(1 + 5.6\tau)\, G_D$ for G_E^n [99], where $\mu_p = 2.79$, $\mu_n = -1.91$, and $\tau = Q^2/(4m_n^2)$. The good agreement of the measured tensor asymmetry A_d^T with the full model supports the calculations of FSI for a reliable extraction of G_E^n from the beam-target vector asymmetry A_{ed}^V at the percent level.

The data were divided into four Q^2 bins to determine G_E^n/G_M^n with a comparable statistical significance. The data were acquired in two separate runs corresponding to a target polarization angle of $31.64° \pm 0.43°$ and $46.32° \pm 0.45°$, respectively. The average product of beam and target polarization determined from the $^2\vec{\mathrm{H}}(\vec{e}, e'p)$ reaction was $P_eP_z = 0.5796 \pm 0.0034(\mathrm{stat}) \pm 0.0034(\mathrm{sys})$ in the first and $0.5149 \pm 0.0043(\mathrm{stat}) \pm 0.0054(\mathrm{sys})$ in the second data set. The systematic error of G_E^n/G_M^n is dominated by the uncertainty of the target spin angle θ_d. Other systematic uncertainties include that of the beam-target polarization product P_eP_z, the accuracy of kinematic reconstruction, as well as the dependency on software cuts. The systematic uncertainties were evaluated individually for each Q^2 bin and data set by combining the uncertaintiess from each source, taking covariances into account; the correlated and uncorrelated uncertainty categories of the two measurements were then combined for a resulting systematic uncertainty of each bin. False asymmetries were studied with the observables A_d^V and A_{ed}^T and found to be consistent with zero. Radiative corrections to the asymmetries calculated in a PWBA formalism using the code MASCARAD [77] are < 1 % and therefore also neglected. The uncertainties of the reaction mechanism and FSI corrections, which are small compared to the experimental uncertainties, are not included in the systematic uncertainty.

Data on G_E^n from double-polarization experiments [70–72, 76, 100, 101] are displayed in Figure 7 along with the results of this work [102]. All of the polarization data were experimentally determined as electric to magnetic form factor ratios. We used a parameterization [27] for G_M^n to determine G_E^n from BLAST and to adjust the previously published values. The data from a variety of experiments are consistent and remove the large model uncertainty of previous G_E^n extractions from elastic electron-deuteron scattering [103]. The new distribution is also in agreement with G_E^n extracted from the deuteron quadrupole form factor [104].

The measured distribution of G_E^n can be parameterized as a function of Q^2 based on the sum of two dipoles, $\sum_i a_i/(1+Q^2/b_i)^2$ $(i=1,2)$, shown as the BLAST fit in Figure 7 (blue line) with a one-sigma error band. With $G_E^n(0)=0$ and the slope at $Q^2=0$ constrained by $\langle r_n^2 \rangle = (-0.1148 \pm 0.0035)$ fm^2 [105].

Details can be found in Reference [102]. The parameterization [72] (magenta dash-dotted line) is based on the form introduced in [27] with the *ansatz* of an additional bump structure around $0.2 - 0.4$ (GeV/c)^2. Also shown are the recent results based on vector meson dominance (VMD) and dispersion relations (red short-dashed [84, 106] and green long-dashed lines [107]), and the prediction of a light-front cloudy bag model with relativistic constituent quarks [28] (cyan dotted line).

The new data from BLAST do not show a bump structure at low Q^2 as previously suggested [27, 72]. The BLAST data are in excellent agreement with dispersion analysis [84, 106, 107] and also agree well with the meson-cloud calculation [28]. The improved precision of the data at low Q^2 provides strong constraints on the theoretical understanding of the nucleon's meson cloud.

3.3 Fourier Transforms of Nucleon Form Factors

Understanding how the electromagnetic form factors for the nucleons arise from the fundamental QCD interaction of quarks and gluons is an important goal for nuclear physics. In addition to the data measured by the BLAST experiment there is now a wealth of data available over a range of Q^2 for all the nucleon form factors which can provide constraints and guidance for theory.

Also, surprisingly, a striking discrepancy has been observed in the ratio of the proton electric to magnetic form factors between measurements using traditional Rosenbluth separation and measurements using polarization transfer [51, 52, 81]. This discrepancy has several consequences. First, it means that the simple dipole model for the proton electric form factor is no longer valid at high Q^2. Second, the explanation for the discrepancy is likely that two photon exchange contributions, previously considered negligible, are in fact significant. The latter issue is being investigated by several groups [108–110]. In any event the discrepancy adds impetus to understanding the nucleon form factors.

One such theoretical approach has been to fit the available low Q^2 form factor data together with the available data from polarization measurements within the framework of the GKex vector dominance model [111, 112]. While phenomenological, the agreement with the data is striking and possibly provides some insight into the role of the vector mesons and the asymptotic Q^2 behavior of QCD in explaining the nucleon form factors. Discussion of the GKex model is beyond the scope of this review but some of the results are shown.

Rather than present the results in momentum space we take the Breit frame Fourier transform of the GKex model fits to the electric form factors and show the relative contributions of the various vector mesons and pQCD. Note that the resulting coordinate space distributions should not be interpreted as "charge distributions" but perhaps some intuitive understanding can be gained. Figure 8 shows the Fourier transform of a fit to the proton electric form factor with mainly contributions from pQCD, ω, ρ, and ω' mesons, which add together to form the total distribution. Figure 9 shows the Fourier transform of the fit to the neutron electric form factor where contributions from pQCD and ρ mesons interfere with those from the ω and ω' mesons to form the total.

4 The Structure of the Deuteron from Elastic Electron Scattering

The deuteron, as the only two-nucleon bound state, plays an important role in the understanding of nucleon-nucleon interactions including short-range properties and non-nucleonic degrees of freedom [113–115].

Precise measurements of elastic deuteron form factors constrain nuclear models, *e.g.* Hamiltonian dynamics [1–3] or explicitly covariant models [], and provide benchmarks for recent developments in Effective Field Theory for low-Q^2 physics [6, 7].

The electromagnetic structure of the deuteron, as observed through elastic electron scattering, can be described by three form factors, G_C, G_Q, and G_M, which are the electric monopole, the electric quadrupole, and the magnetic dipole distributions of the deuteron, respectively, in 4-momentum Q^2 space. In single-photon exchange approximation, the three form factors determine the elastic unpolarized cross section and all of the vector and tensor polarization observables. The latter are fully determined by specifying two of the three possible form factor ratios, *e.g.* G_C/G_Q and G_C/G_M.

Assuming parity and time-reversal invariance and in the one-photon exchange approximation, the unpolarized elastic electron-deuteron cross section is given by $\sigma_0 = \sigma_{\rm Mott} f_{\rm rec}^{-1}\, S$, where $S = A + B\tan^2(\theta_e/2)$. Here,

$$\sigma_{\rm Mott} = (\alpha/2E)^2(\cos(\theta_e/2)/\sin^2(\theta_e/2))^2 \tag{8}$$

is the Mott cross section with the nuclear recoil factor $f_{\rm rec} = 1{+}2(E/M_d)\sin^2(\theta_e/2)$, where E and θ_e denote the electron beam energy and scattering angle, respectively, and M_d the deuteron mass.

From measurements of σ_0 at different scattering angles, two combinations of the deuteron form factors

$$\begin{aligned} A(Q^2) &= G_C^2 + (8/9)\eta^2 G_Q^2 + (2/3)\eta G_M^2 \qquad (9) \\ B(Q^2) &= (4/3)\eta(1+\eta)G_M^2 \qquad (10) \end{aligned}$$

with $\eta = Q^2/(4M_d^2)$, can be derived (Rosenbluth separation). At low Q^2, the cross section is dominated by $A(Q^2)$, and A itself is dominated by G_C. Two issues are apparent: It requires at least one more independent measurement of a polarization observable in order to separate the monopole and quadrupole form factors, G_C and G_Q, for which the tensor analyzing power T_{20} is best suited. Secondly, the smallness of the magnetic contribution to the cross section at low Q^2 limits the precision of the Rosenbluth method to determine G_M. Here, measurements of polarization observables involving the interference of G_M with G_C or with G_Q are of particular interest. The latter interference is probed by the tensor analyzing power T_{21} and the former by the vector analyzing power T_{11}^e, which are both discussed below.

With the availability of both a tensor and vector polarized deuterium target, the polarized cross section can be written as

$$\sigma = \sigma_0 \left[1 + \sqrt{\frac{1}{2}} P_{zz} A_d^T + \sqrt{\frac{3}{2}} P_e P_z A_{ed}^V \right], \tag{11}$$

giving rise to target tensor, A_d^T, and beam-target vector asymmetries, A_{ed}^V. The other possible asymmetries, helicity (A_e), beam-target tensor (A_{ed}^T), and target vector asymmetry (A_d^V), all vanish for symmetry arguments. The longitudinal polarization of the electron is denoted by P_e, the deuteron vector polarization is given by $P_z = n_+ - n_-$, and the tensor polarization by $P_{zz} = n_+ + n_- - 2n_0$, where n_+, n_0 and n_- are the relative populations of the nuclear spin projections $m = +1, 0, -1$ along the direction of polarization, respectively. The non-vanishing asymmetries A_d^T and A_{ed}^V are related to the tensor and vector analyzing powers,

$$\begin{aligned} A_d^T &= \frac{3\cos^2\theta^* - 1}{2} T_{20}(Q^2, \theta_e) - \sqrt{\frac{3}{2}} \sin 2\theta^* \cos\phi^* \, T_{21}(Q^2, \theta_e) \\ &\quad + \sqrt{\frac{3}{2}} \sin^2\theta^* \cos 2\phi^* \, T_{22}(Q^2, \theta_e) \end{aligned} \tag{12}$$

$$A_{ed}^{V} = \sqrt{3}\left[\frac{1}{\sqrt{2}}\cos\theta_e^*\, T_{10}^e(Q^2,\theta_e) - \sin\theta^*\cos\phi^*\, T_{11}^e(Q^2,\theta_e)\right]. \tag{13}$$

Here, the angles θ^* and ϕ^* define the polarization direction in a frame where the z axis is along the direction of the virtual photon and the y axis is defined by the vector product of the incoming and outgoing electron momenta. The tensor analyzing powers T_{20}, T_{21}, T_{22} and vector analyzing powers T_{10}^e, T_{11}^e are in turn related to the three form factors G_C, G_Q, and G_M through

$$T_{20}(Q^2,\theta_e) = -\frac{1}{\sqrt{2}S}\left[\frac{8}{3}\eta G_C G_Q + \frac{8}{9}\eta^2 G_Q^2\right. \tag{14}$$

$$\left. + \frac{1}{3}\eta\left(1 + 2(1+\eta)\tan^2\frac{\theta_e}{2}\right) G_M^2\right] \tag{15}$$

$$T_{21}(Q^2,\theta_e) = -\frac{2}{\sqrt{3}S}\eta\sqrt{\eta\left[1 + (1+\eta)\tan^2\frac{\theta_e}{2}\right]}\, G_M G_Q \tag{16}$$

$$T_{22}(Q^2,\theta_e) = -\frac{1}{2\sqrt{3}S}\eta\, G_M^2 \tag{17}$$

$$T_{10}^e(Q^2,\theta_e) = -\sqrt{\frac{2}{3}}\frac{1}{S}\eta(1+\eta)\tan\frac{\theta_e}{2}\sqrt{\frac{1}{1+\eta} + \tan^2\frac{\theta_e}{2}}\, G_M^2 \tag{18}$$

$$T_{11}^e(Q^2,\theta_e) = \frac{2}{\sqrt{3}S}\sqrt{\eta(1+\eta)}\tan\frac{\theta_e}{2}\, G_M\left[G_C + \frac{\eta}{3}G_Q\right]. \tag{19}$$

Of the tensor analyzing powers, T_{20} is dominant, T_{21} is still significant, while T_{22} is small and treated as a correction in Eq. (12). In particular, the contribution from T_{20} is sizable and quite sensitive to the interference of G_C and G_Q. Knowledge of A, B, and T_{20} can be obtained experimentally with the highest precision and allows for a separation of all three elastic form factors. The tensor analyzing powers T_{20} and T_{21} have been measured with BLAST in the low-Q^2 region covering the minimum of T_{20} and the first node of G_C.

The superscript "e" on T_{10}^e and T_{11}^e indicates that a polarized electron beam as well as a vector polarized target is required to measure these observables. Relative to T_{11}^e, the vector analyzing power T_{10}^e is suppressed at low Q^2 due to the leading dependence on η. This was confirmed by the data indicating that T_{10}^e

is zero within statistical uncertainties (see below). At low Q^2, the factor η also suppresses the contribution from G_Q so that T^e_{11} is dominated by the interference of G_C and G_M. With $A(Q^2)$ dominated by G_C and known at low Q^2 with small uncertainty, T^e_{11} provides a strong lever arm in testing predictions for the magnetic form factor G_M in this region.

In BLAST we have made the first known measurement of the vector analyzing power T^e_{11} in doubly polarized electron deuteron elastic scattering. Prior measurements of T^e_{11} have not been possible due to the absence of experiments which provide both an intense polarized electron beam and a vector polarized deuterium target.

The average target spin angle was calibrated simultaneously with the tensor polarization of the target by comparing the elastic tensor asymmetries at low momentum transfer $1.75 < Q < 2.15\ \mathrm{fm}^{-1}$ to Monte Carlo simulations based on parameterization III of Reference [116] fit to previous experimental data, resulting in $P_{zz} = 0.683 \pm 0.015 \pm 0.013 \pm 0.034$ and $0.563 \pm 0.013 \pm 0.023 \pm 0.028$ for the 2004 and 2005 data sets, respectively, where the three uncertainties are statistical, systematic and due to the parameterization.

Experimentally, one forms A^T_d and A^V_{ed} by particular combinations of charge-normalized yields dependent on beam and target spin state, and after normalizing each raw asymmetry to P_{zz} and $P_e P_z$, respectively. The target tensor asymmetry is derived experimentally as

$$A^T_d = \frac{\sqrt{2}}{P_{zz}} \frac{Y^+ - Y^-}{2Y^+ + Y^-}, \tag{20}$$

where Y^+ and Y^- are the charge-normalized yields with the target in the $T+$ ($m = \pm 1$) and the $T-$ ($m = 0$) state, respectively, averaged over both helicities. With the target polarization vector, θ_T, directed to beam-left, events where the electron wass scattered into the right and left sectors of BLAST corresponded to kinematics where the three-momentum transfer, $\vec{q}$, was approximately parallel and perpendicular to θ_T, respectively. Two asymmetries were measured simultaneously in both sectors, corresponding to θ^* close to 90° and 0°, respectively. A small correction for the contribution of T_{22} was applied based on parameterization III [116], and the analyzing powers T_{20} and T_{21} were extracted from two asymmetries for each Q^2 bin, with event-averaged coefficients in Eq. (12). The results are shown in Figure 10. The values for T_{20} measured in this work are in agreement with previous data, but they are much more precise. The results for T_{21} are somewhat larger in magnitude yet still compatible with previous data within total uncertainties.

The beam-target vector asymmetry was obtained by forming

$$A^V_{ed} = \sqrt{\frac{3}{2}}\,\frac{1}{P_e P_z}\,\frac{y_{++} - y_{-+} - y_{+-} + y_{--}}{y_{++} + y_{-+} + y_{+-} + y_{--} + y_{+0} + y_{-0}}\ , \tag{21}$$

where y_{hm} are charge-normalized spin-dependent yields for combinations of helicity $h = \pm 1$ and magnetic target quantum number $m = \pm 1$ and 0. Again, two asymmetries with $\theta^* \approx 90°$ and 0° were measured simultaneously with electrons scattered into the left and right sectors of BLAST, allowing the extraction of the vector analyzing power T^e_{11}. With regard to T^e_{10}, the large relative uncertainty on this observable precluded a statistically significant measurement in the current experiment. The extracted values for T^e_{11} as measured by BLAST are shown in Figure 11.

From Figure 11 one can see that the BLAST data for T^e_{11} provide a constraint on theoretical descriptions below $Q^2 < 0.4$ (GeV/c)^2. In both Figures 10 and 11, the good agreement of BLAST data for the tensor and vector analyzing powers with the non-relativistic model with meson exchange and relativistic corrections by Arenhövel *et al.* [1] is evident. This is also true of Phillips' Effective Field Theory calculation [7] in this low Q^2 region. In addition, the good agreement of the BLAST results with parameterization III of the deuteron form factors and structure functions by Abbott [116] is displayed.

The significant sources of systematic errors in the measurements of the tensor and vector analyzing powers were the uncertainties in the reconstructed electron scattering angle θ_e, in the orientation of the target polarization vector, and in the tensor polarization and beam-target vector polarization product.

In conclusion, BLAST has provided a high-precision measurement of the tensor analyzing powers T_{20} and T_{21} over a wide Q^2 range, as well as the first measurement of the vector analyzing power T_{11}^e.

5 Electro-disintegration of the Deuteron with Detection of an Emitted Proton

During data taking on the polarized deuteron target, large numbers of events were accumulated in which both a scattered electron and an emitted proton were detected. The cross section for such events was sensitive to a number of interesting aspects of the photo-nucleon interaction and to the dynamics of deuteron structure: the quasi-elastic electron-proton interaction; final state interactions; meson exchange currents; relativistic effects; isobar configurations; and the amount of D-state in the deuteron wave function. By using the large acceptance of the BLAST spectrometer and asymmetries related to the polarization of the beam and target, it was possible to use the $^2\vec{\mathrm{H}}(\vec{e}, e'p)$ data to emphasize one or more of these aspects and to test models of nucleon-nucleon interactions.

As has been indicated in other sections, the polarization direction of the target was chosen so that the virtual photon from the scattered electron was roughly along (parallel kinematics) or normal to (perpendicular kinematics) the polarization of the struck deuteron.

Because both the beam and target were polarized, it was possible to measure experimental asymmetries depending on polarization directions and detection directions. The two asymmetries of relevance to this discussion are the tensor asymmetry A_d^T and the beam-vector asymmetry A_{ed}^V. Both follow from the cross section formula:

$$\begin{aligned}
\sigma &= \sigma_0[1 + \sqrt{\frac{3}{2}} P_z A_{ed}^V + \sqrt{\frac{1}{2}} P_{zz} A_d^T + \\
&\quad P_e(A_e + \sqrt{\frac{3}{2}} P_z A_{ed}^V + \sqrt{\frac{1}{2}} P_{zz} A_d^T)] \qquad (22) \\
A_d^T &= \frac{\sqrt{2}}{12 P_{zz} \sigma_0}[\sigma(P_e, P_z, P_{zz}) + \sigma(-P_e, P_z, P_{zz}) + \sigma(P_e, -P_z, P_{zz}) + \\
&\quad \sigma(-P_e, -P_z, P_{zz}) - 2[\sigma(P_e, 0, -2P_{zz}) + \sigma(-P_e, 0, -2P_{zz})]] \qquad (23) \\
A_{ed}^V &= \frac{\sqrt{2}}{4\sqrt{3} P_z \sigma_0}[\sigma(P_e, P_z, P_{zz}) - \sigma(-P_e, P_z, P_{zz}) - \\
&\quad \sigma(P_e, -P_z, P_{zz}) - \sigma(-P_e, -P_z, P_{zz})] \qquad (24)
\end{aligned}$$

where σ_0 is the unpolarized cross section, P_e is the beam helicity, and P_z and P_{zz} are the vector and tensor polarizations of the deuteron target.

The vector polarization of the deuteron target was determined by measuring the vector asymmetry and fitting this to the theoretical prodiction at low missing momentum. The tensor asymmetry and the beam-vector asymmetry have different sensitivities to the various aspects of the electron-nucleon interaction and deuteron structure. Data for both the tensor asymmetry and the beam-vector asymmetry are shown in Figures 12 and 13.

The asymmetries are plotted as functions of missing momentum for both perpendicular kinematics and parallel kinematics and contain data for Q^2 between

0.1 and 0.2 GeV/c^2. In fact asymmetries corresponding to Q^2 up to 0.5 GeV/c^2 were measured with BLAST, but with increasingly poorer statistics.

The theoretical model predictions shown in Figs. 12 and 13 come from the formalism of Arenhövel et al [97, 98], who used the Bonn [117, 118], V18 [2, 3], and Paris [119] potentials. It was found that there were no significant differences between predications using the three different potentials, and the Bonn potential was used for comparison with the data shown in the Figures. Theoretical curves were calculated, in addition to the simple Plane Wave Born Approximation (PWBA), with inclusion consecutively of final state interactions, meson exchange currents, isobar configurations, and relativistic corrections.

One can make the following observations concerning the measured asymmetries and the comparison to theoretical calculations:

1. The tensor asymmetry is consistent with zero at very low missing momenta, as expected, and generally rises with increasing missing momentum.
2. The beam-vector asymmetry is constant at very low missing momenta, and generally rises with increasing missing momentum.
3. The agreement between the data and the Bonn potential predictions is good, and it is clear that including corrections for final state interactions, meson exchange currents, relativistic effects, and isobar currents is important to achieve this agreement.
4. It should be noted that, although not shown in these figures, at higher Q^2 the data, especially for the beam-vector asymmetry, are higher than predicted by the model. One possibility for this discrepancy is the fact that in the comparison free nucleon form factors were used; the form factors for bound nucleons may of course be somewhat different.

From these coincidence data, using especially the polarization flexibilities of the beam and targets, one can have confidence that the overall interaction of electrons with bound nucleons in the deuteron is well-understood.

6 Summary and Conclusions

The measurements described here have provided important new information on the nucleon elastic form factors at low momentum transfers. They provide essential data to constrain the distribution of the charge and magnetism at long distance scales. In particular the BLAST data on the neutron charge distribution, together with other recent measurements using spin observables, provide a long-awaited determination of the neutron charge form factor with precision comparable to that of the proton form factor. The data from BLAST on the deuteron provide new, precise constraints for theoretical models of few-body structure.

Finally, the success of the BLAST experimental program validates the uniqueness and utility of the technique of windowless gas target and large acceptance detector with an intense electron beam to study elastic electron-nucleon scattering. This technique is being pursued by the OLYMPUS experiment at DESY [120] to determine the contributions beyond single-photon exchange and is under consideration at Jefferson Lab [121] for a search for the A$'$ boson.

7 Acknowledgments

The authors would like to acknowledge the contributions of the entire BLAST collaboration in the successful realization of the experiment and the outstanding efforts of the MIT-Bates staff in the delivery of high-quality beam and for technical support. We would also like to thank H. Arenhövel, T.W. Donnelly and

D. Phillips for theoretical support of the BLAST data analysis. The authors' research is supported by the U.S. Department of Energy and the National Science Foundation.

References

1. Arenhovel H, Ritz F, Wilbois T, Phys.Rev. C61:034002 (2000), nucl-th/9910009.
2. Wiringa RB, Stoks V, Schiavilla R, Phys.Rev. C51:38 (1995), nucl-th/9408016.
3. Schiavilla R, Pandharipande V, Phys.Rev. C65:064009 (2002), nucl-th/0201043.
4. Van Orden J, Devine N, Gross F, Phys.Rev.Lett. 75:4369 (1995).
5. Phillips DR, Wallace SJ, Devine N, Phys.Rev. C58:2261 (1998), nucl-th/9802067.
6. Phillips DR, Higher order calculations of electron deuteron scattering in nuclear effective theory, 2003, nucl-th/0304046.
7. Phillips DR, J. Phys. G34:365 (2007), nucl-th/0608036.
8. William H. Bates Linear Accelerator Center, Pulse Stretcher Ring, Proposal for a CW Upgrade, 1984.
9. BLAST Collaboration, BLAST Technical Design Report, 1997.
10. Crawford C, *Precision Measurement of the Proton Electric to Magnetic Form Factor Ratio with BLAST*, PhD thesis, Massachusetts Institute of Technology, 2005.

11. Sindile A, *Proton Form Factor Ratio Measurement with BLAST*, PhD thesis, University of New Hampshire, 2006.
12. Ziskin V, *Measurement of the Electric Form Factor of the Neutron at Low Momentum Transfers Using a Vector Polarized Deuterium Gas Target at BLAST*, PhD thesis, Massachusetts Institute of Technology, 2005.
13. Geis E, *The Electric Form Factor of the Neutron at Low Momentum Transfers as Measured at Bates Large Acceptance Spectrometer Toroid*, PhD thesis, Arizona State University, 2007.
14. Zhang C, *Measurement of Tensor Analyzing Powers in Elastic Electron Deuteron Scattering with BLAST*, PhD thesis, Massachusetts Institute of Technology, 2006.
15. Karpius P, *Vector Polarization Observables of the Deuteron and A New Measurement of the Magnetic Dipole Form Factor G_M*, PhD thesis, University of New Hampshire, 2005.
16. Maschinot A, *Analysis of Scattered Protons in Deuteron Electrodisintegration with a Polarized Electron Beam and an Internal Polarized Target*, PhD thesis, Massachusetts Institute of Technology, 2005.
17. Degrush A, *Single and Double Polarization Observables in the Electrodisintegration of the Deuteron from BLAST*, PhD thesis, Massachusetts Institute of Technology, 2010.
18. Meitanis N, *A Measurement of the Neutron Magnetic Form Factor G_M^n from Quasi-elastic $^2\vec{\mathrm{H}}(\vec{e},e')$ at Low Q^2*, PhD thesis, Massachusetts Institute of Technology, 2006.
19. Filoti O, *Inclusive Scattering of Polarized Electrons from Polarized Protons*

in the Δ-Excitation Region with BLAST, PhD thesis, University of New Hampshire, 2007.

20. Xiao Y, *A Study of the Spin Dependence of Pion Electroproduction near the Δ Region*, PhD thesis, Massachusetts Institute of Technology, 2009.
21. Hasell D, et al., Nucl. Instrum. Meth. A603:247 (2009).
22. Farkhondeh M, Franklin W, Tsentalovich E, Zwart T, Ihloff E, MIT-Bates Polarized Source, volume 675 of *American Institute of Physics Conference Series*, pp. 1098–1102, 2003.
23. Franklin WA, The MIT-Bates Compton Polarimeter for the South Hall Ring, p. 714, 2004.
24. Cheever D, et al., Nucl. Instrum. Meth. A556:410 (2006).
25. Tonguc B, Alarcon R, Botto T, Calarco J, Degrush A, et al., Nucl. Instrum. Methods A 553:364 (2005).
26. Faessler A, Gutsche T, Lyubovitskij VE, Pumsa-ard K, Phys. Rev. D73:114021 (2006).
27. Friedrich J, Walcher T, Eur. Phys. J. A17:607 (2003).
28. Miller GA, Phys. Rev. C66:032201(R) (2002).
29. Alkofer R, Holl A, Kloker M, Krassnigg A, Roberts CD, Few Body Syst. 37:1 (2005).
30. Holl A, et al., Nucl. Phys. A755:298 (2005).
31. Kelly JJ, Phys. Rev. C66:065203 (2002).
32. Schindler MR, Gegelia J, Scherer S, Eur. Phys. J. A26:1 (2005).
33. Scherer S, Prog. Part. Nucl. Phys. 64:1 (2010).

34. LHPC, Bratt JD, et al., Phys. Rev. D82:094502 (2010).
35. Yamazaki T, et al., Phys. Rev. D79:114505 (2009).
36. Hagler P, Phys. Rept. 490:49 (2010).
37. G0, Armstrong DS, et al., Phys. Rev. Lett. 95:092001 (2005).
38. HAPPEX, Acha A, et al., Phys. Rev. Lett. 98:032301 (2007).
39. Pohl R, et al., Nature 466:213 (2010).
40. Mohr PJ, Taylor BN, Rev. Mod. Phy. 80:633 (2008).
41. A1, Bernauer JC, et al., Phys. Rev. Lett. 105:242001 (2010).
42. Gao H, Int. J. Mod. Phys. E12:1 (2003).
43. Hyde-Wright C, de Jager C, Ann. Rev. Nucl. Part. Sci. 54:217 (2004).
44. Perdrisat CF, Punjabi V, Vanderhaeghen M, Prog. Part. Nucl. Phys. 59:694 (2007).
45. Rosenbluth MN, Phys. Rev. 79:615 (1950).
46. Walker RC, Filippone BW, Jourdan J, Milner R, McKeown R, et al., Phys. Rev. D 49:5671 (1994).
47. Andivahis L, et al., Phys. Rev. D50:5491 (1994).
48. Donnelly TW, Raskin AS, Annals Phys. 169:247 (1986).
49. Arnold RG, Carlson CE, Gross F, Phys. Rev. C23:363 (1981).
50. Jones MK, et al., Phys. Rev. Lett. 84:1398 (2000).
51. Gayou O, et al., Phys. Rev. Lett. 88:092301 (2002).
52. Puckett AJR, et al., Phys. Rev. Lett. 104:242301 (2010).
53. Christy ME, et al., Phys. Rev. C70:015206 (2004).

54. Qattan IA, et al., Phys. Rev. Lett. 94:142301 (2005).
55. Belitsky AV, Ji Xd, Yuan F, Phys. Rev. D69:074014 (2004).
56. Ralston JP, Jain P, (2002), hep-ph/0207129.
57. Ralston JP, Buniy RV, Jain P, (2002), hep-ph/0206063.
58. Miller GA, Frank MR, Phys. Rev. C65:065205 (2002).
59. Brodsky SJ, Hiller JR, Hwang DS, Karmanov VA, Phys. Rev. D69:076001 (2004).
60. Blunden PG, Melnitchouk W, Tjon JA, Phys. Rev. Lett. 91:142304 (2003).
61. Blunden PG, Melnitchouk W, Tjon JA, Phys. Rev. C72:034612 (2005).
62. Chen YC, Afanasev A, Brodsky SJ, Carlson CE, Vanderhaeghen M, Phys. Rev. Lett. 93:122301 (2004).
63. Afanasev AV, Merenkov NP, Phys. Rev. D70:073002 (2004).
64. Crawford CB, et al., Phys. Rev. Lett. 98:052301 (2007).
65. Xu W, et al., Phys. Rev. Lett. 85:2900 (2000).
66. Xu W, et al., Phys. Rev. C67:012201 (2003).
67. Anderson B, et al., Phys. Rev. C75:034003 (2007).
68. Lachniet J, et al., Phys. Rev. Lett. 102:192001 (2009).
69. Kopecky S, Riehs P, Harvey JA, Hill NW, Phys. Rev. Lett. 74:2427 (1995).
70. Plaster B, et al., Phys. Rev. C73:025205 (2006).
71. Madey R, et al., Phys. Rev. Lett. 91:122002 (2003).
72. Glazier DI, et al., Eur. Phys. J. A24:101 (2005).
73. Ostrick M, et al., Phys. Rev. Lett. 83:276 (1999).

74. Herberg C, et al., Eur. Phys. J. A5:131 (1999).

75. Warren G, et al., Phys. Rev. Lett. 92:042301 (2004).

76. Zhu H, et al., Phys. Rev. Lett. 87:081801 (2001).

77. Afanasev A, Akushevich I, Merenkov N, Phys. Rev. D64:113009 (2001).

78. Milbrath BD, et al., Phys. Rev. Lett. 80:452 (1998, Erratum-ibid.82:2221,1999.).

79. Dieterich S, et al., Phys. Lett. B500:47 (2001).

80. Pospischil T, et al., Eur. Phys. J. A12:125 (2001).

81. Punjabi V, et al., Phys. Rev. C71:055202 (2005, Erratum-ibid.C71:069902,2005.).

82. Holzwarth G, Z. Phys. A356:339 (1996).

83. Cardarelli F, Simula S, Phys. Rev. C62:065201 (2000).

84. Lomon EL, Phys. Rev. C66:045501 (2002).

85. Hammer HW, Drechsel D, Meissner UG, Phys. Lett. B586:291 (2004).

86. Janssens T, Hofstadter R, Hughes EB, Yearian MR, Phys. Rev. 142:922 (1966).

87. Price LE, et al., Phys. Rev. D4:45 (1971).

88. Berger C, Burkert V, Knop G, Langenbeck B, Rith K, Phys. Lett. B35:87 (1971).

89. Bartel W, et al., Nucl. Phys. B58:429 (1973).

90. Borkowski F, Peuser P, Simon GG, Walther VH, Wendling RD, Nucl. Phys. A222:269 (1974).

91. Bosted PE, et al., Phys. Rev. C42:38 (1990).

92. Bartel W, Dudelzak B, Krehbiel H, McElroy JM, Meyer-Berkhout U, et al., Phys. Rev. Lett. 17:608 (1966).
93. Stein S, et al., Phys. Rev. D12:1884 (1975).
94. Niculescu C, , PhD thesis, Hampton University, 1999.
95. Arrington J, Phys. Rev. C69:022201 (2004).
96. Zhan X, private communication.
97. Arenhoevel H, Leidemann W, Tomusiak EL, Phys. Rev. C46:455 (1992).
98. Arenhoevel H, Leidemann W, Tomusiak EL, Z. Phys. A 331:123 (1988).
99. Galster S, et al., Nucl. Phys. B32:221 (1971).
100. Eden T, et al., Phys. Rev. C50:R1749 (1994).
101. Passchier I, et al., Phys. Rev. Lett. 82:4988 (1999).
102. Geis E, et al., Phys. Rev. Lett. 101:042501 (2008).
103. Platchkov S, et al., Nucl. Phys. A510:740 (1990).
104. Schiavilla R, Sick I, Phys.Rev. C64:041002 (2001), nucl-ex/0107004.
105. Kopecky S, et al., Phys. Rev. C56:2229 (1997).
106. Lomon EL, Phys. Rev. C64:035204 (2001).
107. Belushkin MA, Hammer HW, Meissner UG, Phys. Rev. C75:035202 (2007).
108. JLab Report No., , 2004 (unpublished).
109. Arrington J, Dmitriev V, Holt R, Nikolenko D, Rachek I, et al., (2004).
110. MIT Report No., , 2009 (unpublished).
111. Crawford C, et al., (2010).
112. Lomon EL, (2006).

113. Carlson J, Schiavilla R, Rev. Mod. Phys. 70:743 (1998).

114. Garcon M, Van Orden JW, Adv. Nucl. Phys. 26:293 (2001), nucl-th/0102049.

115. Gilman RA, Gross F, J. Phys. G28:R37 (2002), nucl-th/0111015.

116. JLAB t20, Abbott D, et al., Eur. Phys. J. A7:421 (2000), nucl-ex/0002003.

117. Machleidt R, Holinde K, Elster C, Phys. Rept. 149:1 (1987).

118. Machleidt R, Phys. Rev. C63:024001 (2001), nucl-th/0006014.

119. Lacombe M, et al., Phys. Rev. C21:861 (1980).

120. The OLYMPUS Collaboration, A Proposal to DESY to Definitively Determine the Contribution beyond Single Photon Exchange, 2008.

121. The DarkLight Collaboration, A Proposal for the DarkLight Experiment at the Jefferson Laboratory Free Electron Laser, 2010.

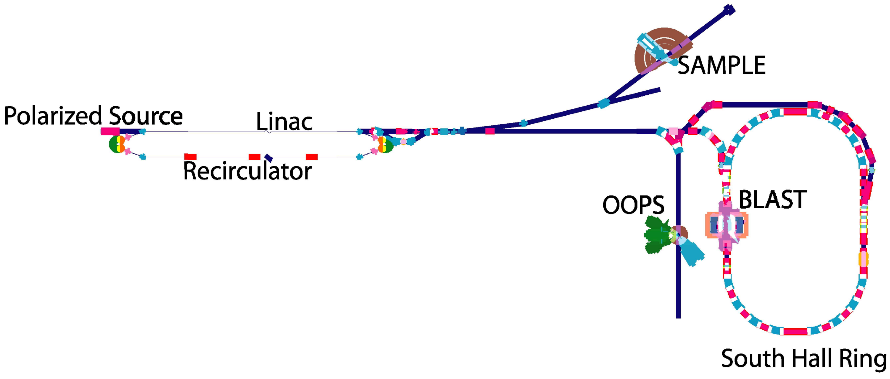

Figure 1: Schematic layout of the MIT-Bates Linear Accelerator Center.

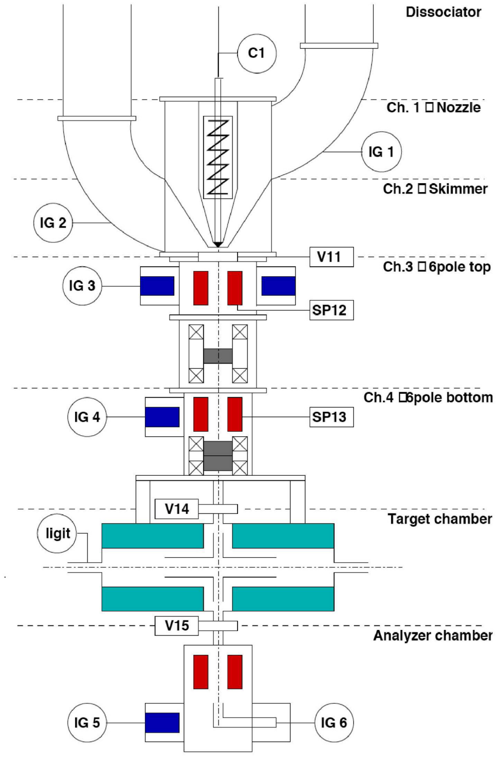

Figure 2: Schematic of the BLAST atomic beam source, the internal target, and Breit-Rabi polarimeter.

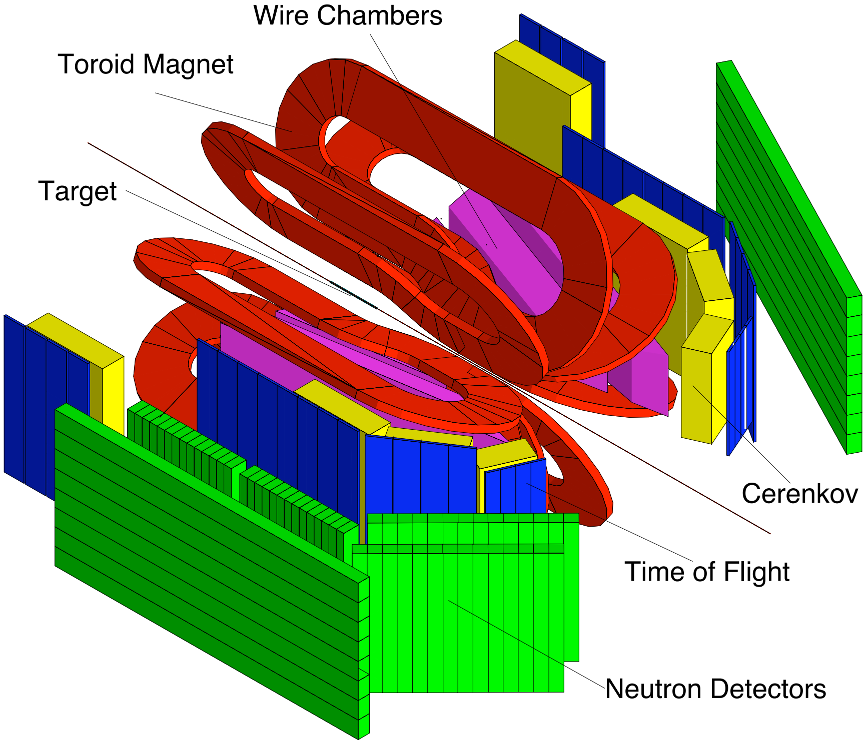

Figure 3: Schematic of the BLAST detector showing the main detector elements.

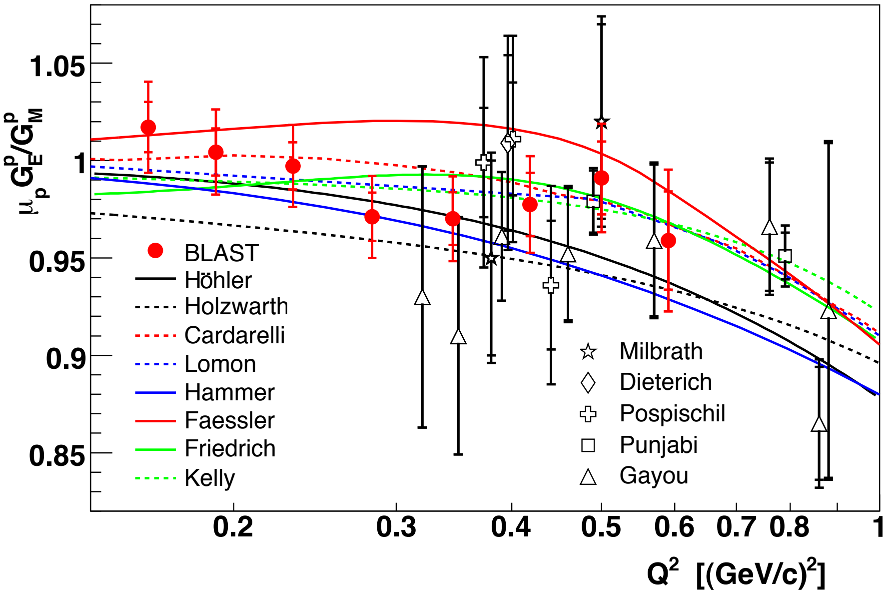

Figure 4: Results of $\mu_p G_E^p/G_M^p$ shown with the world polarized data and several theoretical models.

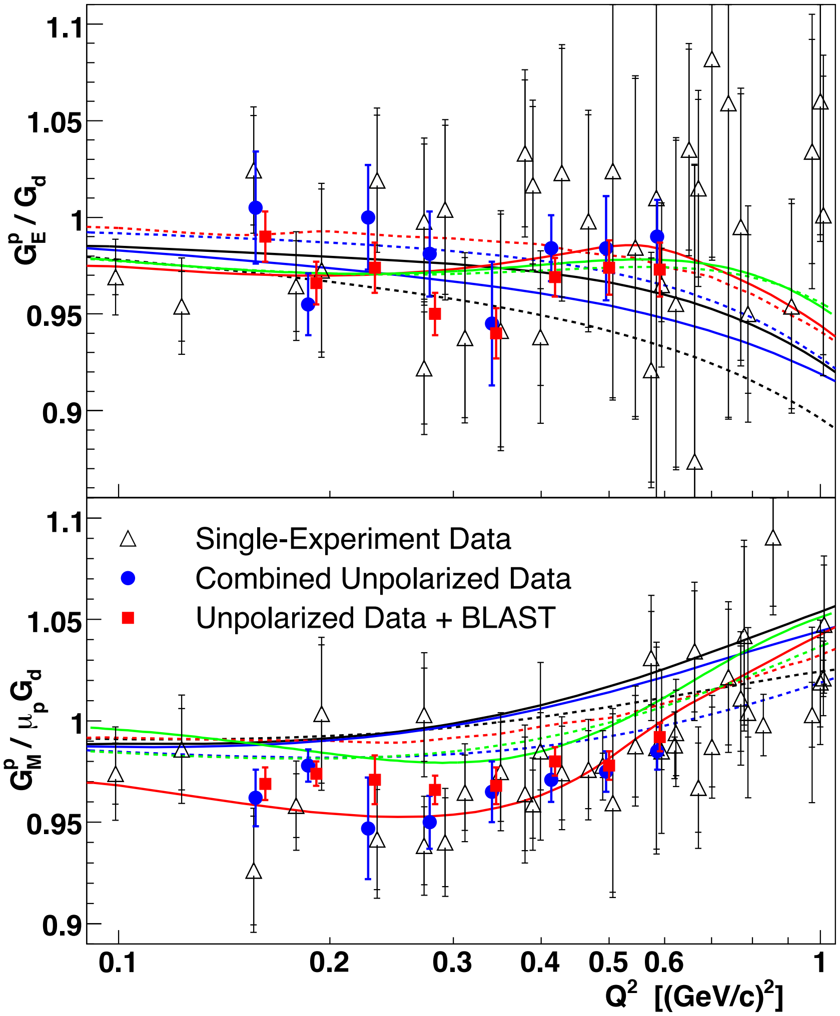

Figure 5: Compilation of world data on G_E^p/G_D and $G_M^p/\mu_p G_D$ at BLAST kinematics with (red) and without (blue) BLAST input, shown with total uncertainties. The curves are the same as in Figure 4.

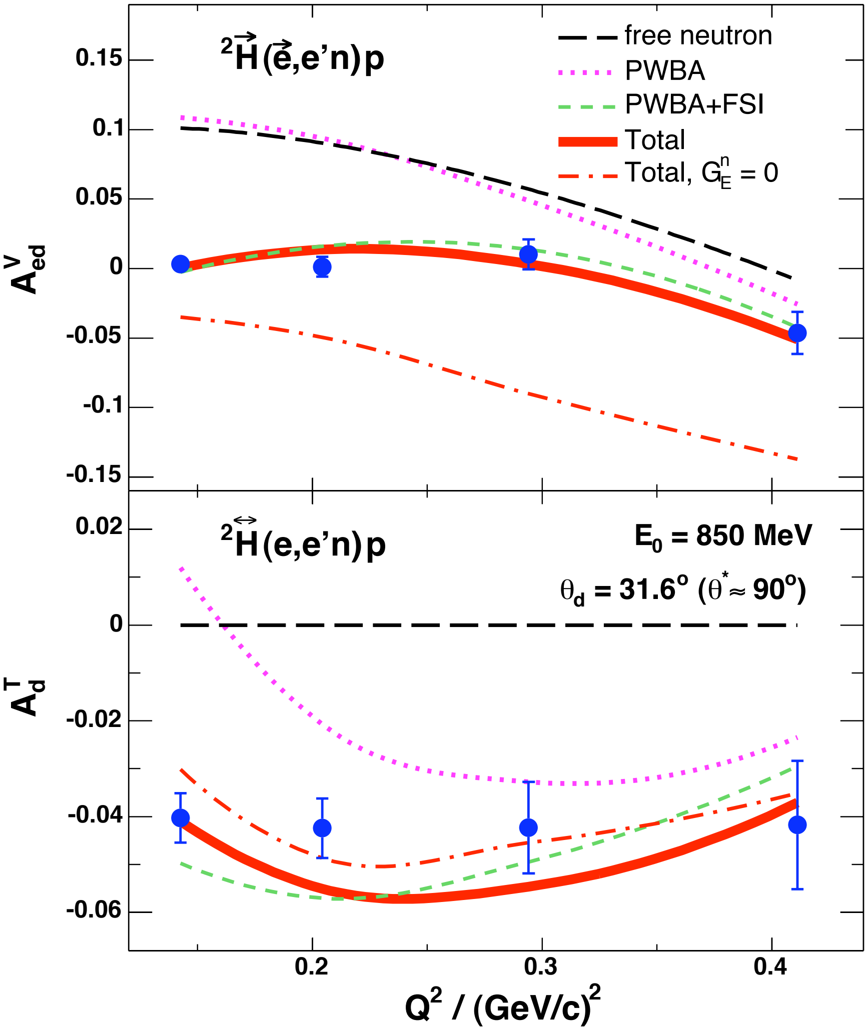

Figure 6: Measured (solid blue points) and calculated beam-target vector polarization observable A_{ed}^V (upper panel) and tensor asymmetry A_d^T (lower panel) for the $^2\mathrm{H}(e, e'n)p$ reaction at 850 MeV.

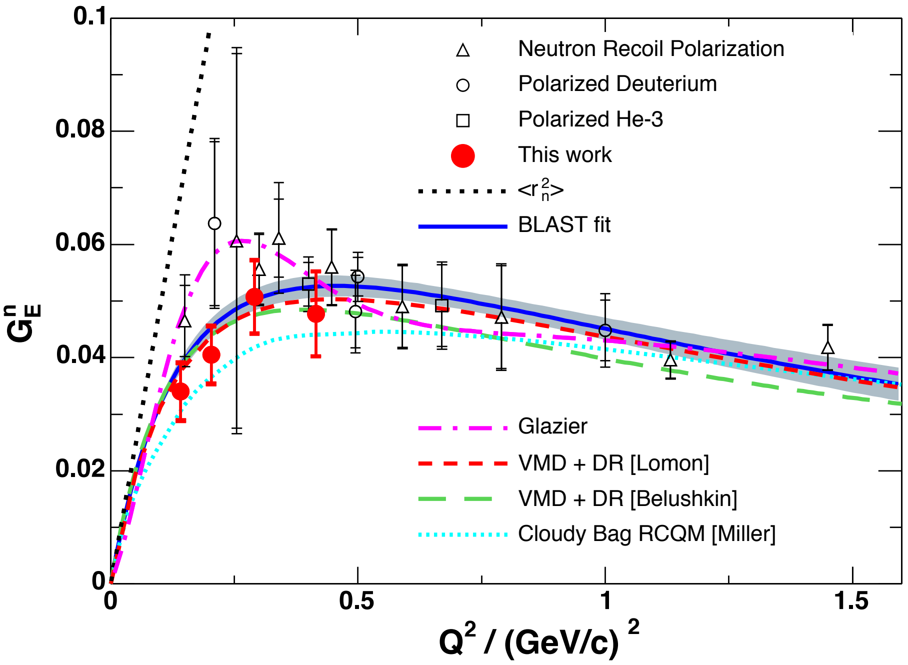

Figure 7: World data on G_E^n from double-polarization experiments. The curves are described in the text.

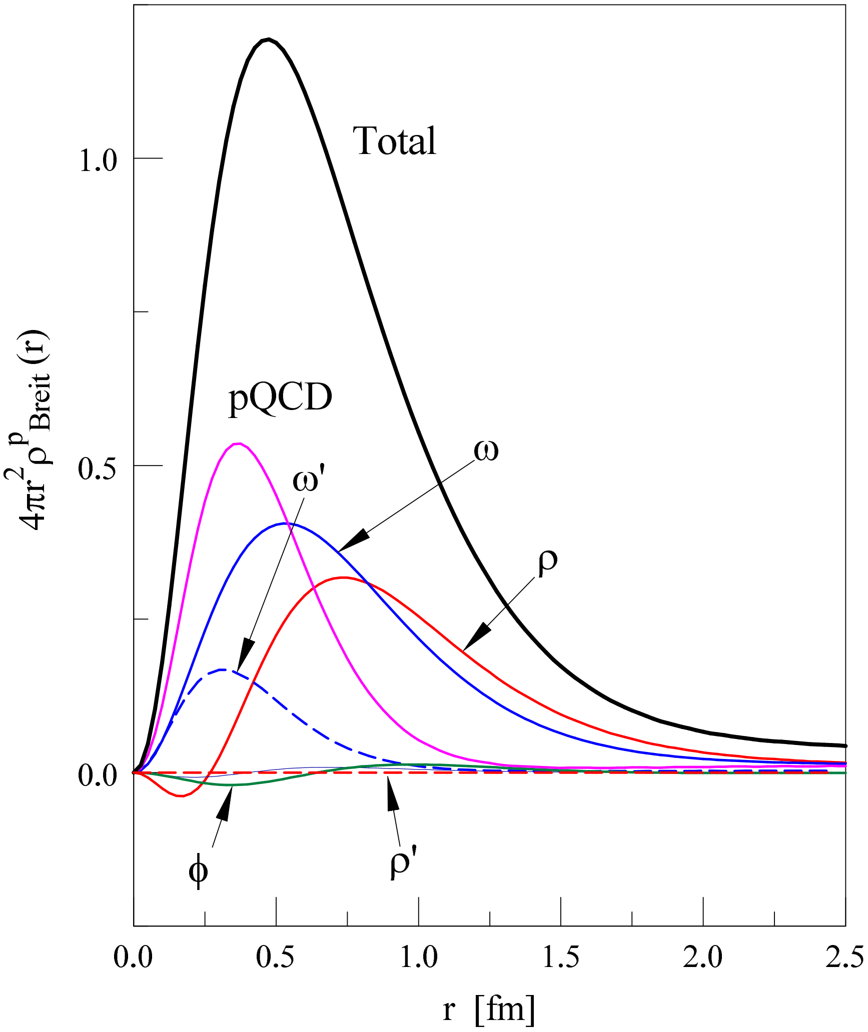

Figure 8: $4\pi r^2 \rho^p_{Breit}(r)$ showing the relative contributions of the various vector mesons from the GKex model together with the pQCD contribution.

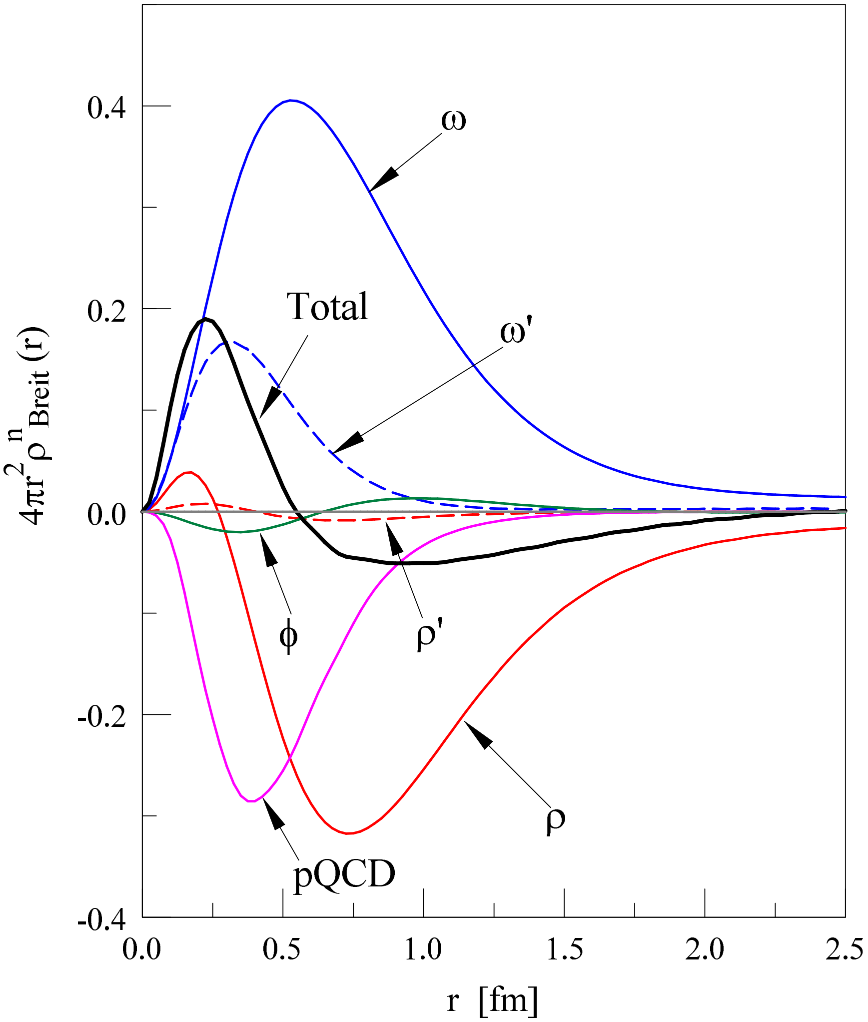

Figure 9: $4\pi r^2 \rho^n_{Breit}(r)$ showing the relative contributions of the various vector mesons from the GKex model together with the pQCD contribution.

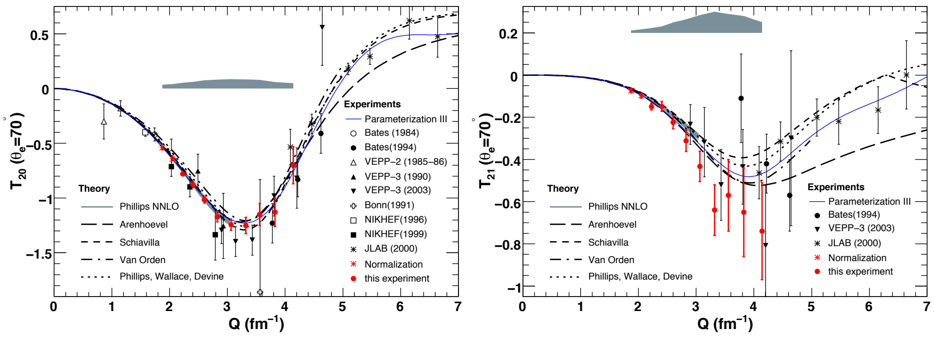

Figure 10: Results for the tensor analyzing powers T_{20} and T_{21} (red dots) in comparison to previous data and various theoretical predictions.

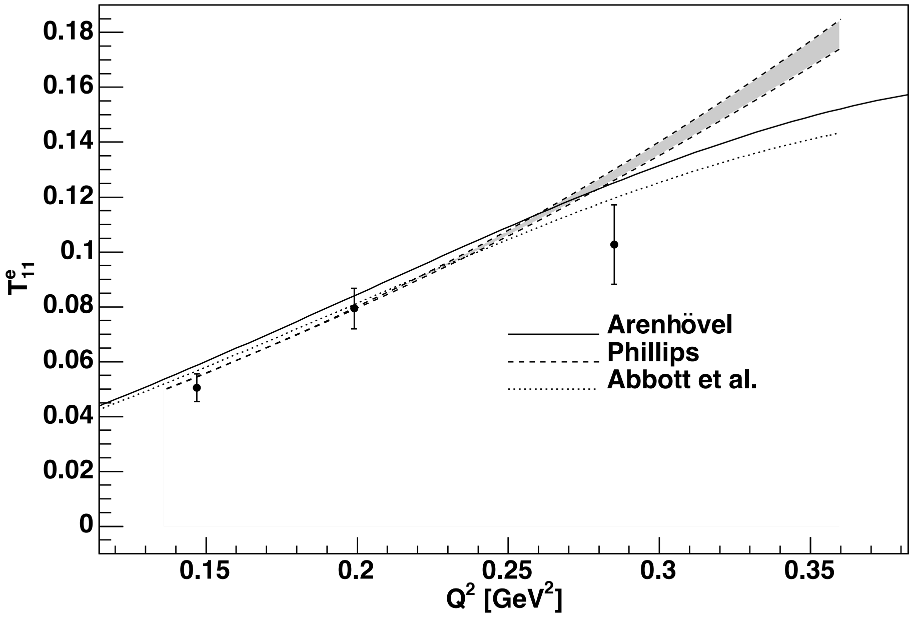

Figure 11: Vector analyzing power T^e_{11}. The theory curves are described in the text.

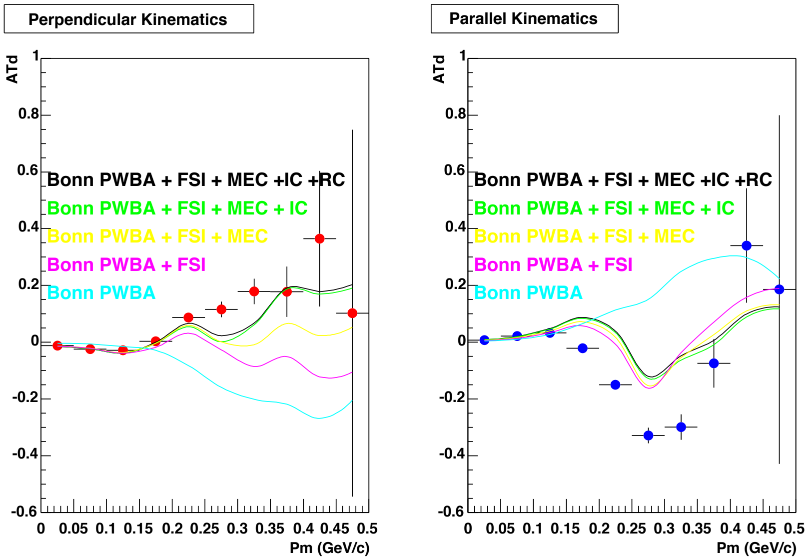

Figure 12: Tensor asymmetry versus missing momentum.

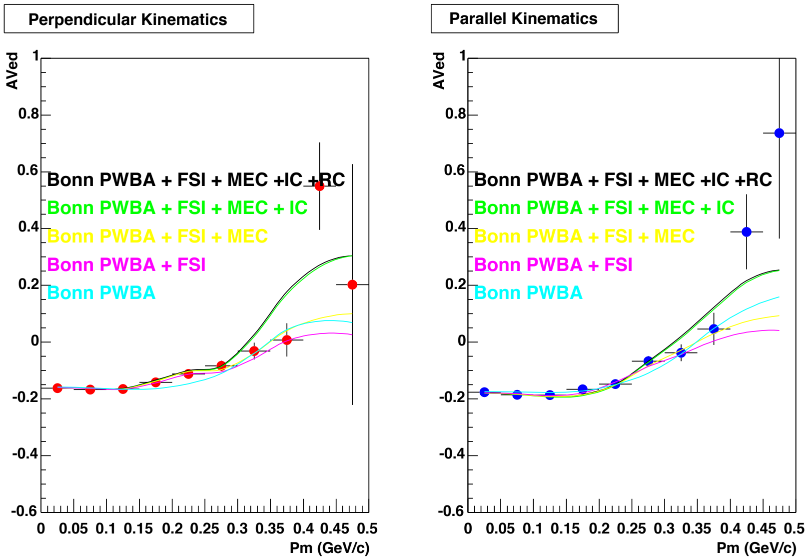

Figure 13: Vector asymmetry versus missing momentum.